Aerodynamic Drag and Stability Characterisation of a Rigid Parachute

Koh Shan Jun[1], Leedon Yong Zheng Rong[2], Lee Jian Ming[3]

[1]Raffles Girls' School, 2 Braddell Rise Singapore 318871
[2]St. Joseph's Institution, 38 Malcolm Road Singapore 308274
[3]DSO National Laboratories, 12 Science Park Drive Singapore 118225

Abstract: This paper presents a comprehensive study on the drag and stability performance of a rigid parachute characterised by the vent ratio, canopy size and angle of attack, \using a combined approach of Computational Fluid Dynamics (CFD) simulations using SST K-Omega turbulence physical drop-test experiments. CFD simulations were conducted to obtain numerical results for drag forces, pressure gradient, and flow patterns surrounding the parachute, considering the rigid nature of the parachute and incorporating realistic environmental conditions, providing a detailed insight into the aerodynamic forces acting on the parachute during descent. To investigate the real-world applicability, a series of drop-tests were performed.

1. Introduction

Parachutes have evolved into indispensable tools across different applications, from recreational skydiving to aeronautical missions, playing a pivotal role in ensuring the safety and success of various operations. The development and optimisation of parachute systems produce challenges such as traditional wind tunnel testing, while highly effective, pose a high financial challenge and as such, have led researchers to explore numerical simulations to predict parachute performance, validated through experimental testing. The motivation behind this study arises from the increasing demand for parachute systems to be tailored to address diverse conditions, from stratospheric altitudes explored by NASA, to high speeds at varying atmospheric conditions, parachutes are expected to adapt to such environments, which highlights the significance of the drag and stability analysis of a parachute.

1.2 Model Development

According to Newton's Second Law, F=ma, the following equation can be derived as,

$$F = mg - F_D = m\frac{dV_G}{dt} \tag{1}$$

Considering the velocities in the body fixed frame,

$$a = \frac{dV_G}{dt} = \frac{d\underline{V}}{dt}\Big|_B + \underline{\omega} \times \underline{V} \tag{2}$$

Substituting back into (1), we obtain the following force equation in the body fixed frame,

$$F = m\frac{d\underline{V}}{dt}|_B + \underline{\omega} \times \underline{V} \tag{3}$$

Identifying the 2 key external forces that act on the body during the gliding stage, the aerodynamic force and the gravitational force acting on the body in the earth fixed inertial frame. As we consider forces about the body fixed frame, the gravitational force is hence taken as,

$$F^b_{gravity} = F^e_{gravity} R_t = mg \begin{bmatrix} -sin(\theta) \\ sin(\phi)cos(\theta) \\ cos(\phi)cos(\theta) \end{bmatrix} \tag{4}$$

Thus, our final force equation can be expressed as

$$F^b_{gravity} + F_a = m \times \frac{d\underline{V}}{dt} + m\underline{\omega} \times \underline{V} \tag{5}$$

Consider the moment of the parachute in the body-fixed frame, where H is the angular momentum of the rigid body which is calculated using $\underline{H} = I\underline{\omega}$.

$M_a = \Sigma_i \ \underline{M_i} = \frac{d\underline{H}}{dt}$ (6)

$$M_a = \Sigma_i \ \underline{M_i} = \frac{d\underline{H}}{dt} \tag{6}$$

Where ω is the angular velocity vector about the centre of mass and I, is the moment of inertia. Thus, this allows us to express the angular momentum of the parachute in each axis as

$$M_a = \frac{d\underline{H}}{dt} + \underline{\omega} \times \underline{H} \tag{7}$$

A study conducted on the Six-Degree-of-Freedom Model of a Controlled Circular Parachute (Dobrokhodov et al., 2003) provided detailed analyses of the shortcomings in existing modelling studies as well as a detailed description of the development of a six-degree-of-freedom parachute model. The 2 key shortcomings were that the apparent mass terms were estimated empirically for axisymmetric shapes and studies only considered the aerodynamics of a fully deployed and symmetric canopy. Studies had shown that the dynamic performance of parachutes was substantially influenced by different apparent mass terms.

The model was developed using the parameters and geometry of a G-12 parachute and A-22 delivery container. It was assumed that the parachute and payload box were rigid, only experienced gravitational and aerodynamic forces, the aerodynamic forces and moments acted about the centre of pressure of the canopy, aerodynamic forces generated by the payload were negligible and the undistorted canopy was symmetrical along the z axis. The final model performed

well when compared against flight-test data while improvements could be made regarding the model identification procedure and accounting for ADS asymmetry.

2. Literature review

2.1 Drag Analysis

Drag analysis is a weak function of the speed of descent and decreases exponentially at higher velocities, influenced by a combination of factors, including the Reynolds number at high speeds and changes to the canopy during high speeds.

2.21 Effects of vortex shedding on drag coefficient

The numerical study conducted by Natarajan and Acrivos concludes that at a Reynolds number of 105, the wake of a sphere becomes unstable, and the study by Sakamoto and Hanio concludes that at a Reynolds number of about 350, the vortices begin to shed periodically. At a Reynolds number exceeding 6000, the vortex sheet separates from the surface as the flow becomes turbulent.

The drag coefficient decreases as a result at higher Reynolds numbers, due to the formation of wakes from the vortex shedding occurring at high Reynolds number. Vortex shedding enables the delay of flow separation as the increased kinetic energy overcomes the adverse pressure gradient. Therefore, the delayed flow separation decreases the pressure drag and the overall drag experienced by the parachute.

2.3 Stability Analysis

Barnhardt and Gidzakl employed a rigid parachute model in their investigation of the effect of wake vortices on flow stability, and concluded that an interaction between the wake and the canopy shock results in a highly unsteady flow around the parachute. Xue and Nishiyama found that the interaction further causes pressure within the canopy to fluctuate at a large amplitude, causing an upstream propagation and lateral expansion of the wake to exhibit an unsteady pulsation.

3. Methodology

3.1 Parameters

The effects of 2 key parameters on the drag and stability of a hemispherical parachute were studied. The first parameter, canopy size, was defined as the reference area of the parachute and was investigated by varying the diameter of the canopy from 65.2cm to 85.2cm. The second parameter, vent ratio, refers to the ratio of the area of the vent hole to the reference area of the canopy and was varied from 0% to 7%.

3.2 Assumptions

Similar to some of the studies reviewed, several key assumptions were made in order to simplify the tests. Firstly, it was assumed that the aerodynamic forces acting on the suspension lines and payload were negligible as highly complex calculations and simulations would be required to accurately study such aerodynamic forces. Secondly, it was assumed that the parachute was a rigid bluff body, experiencing only gravity and aerodynamic forces during the drop-test. The aerodynamic forces experienced by the payload are assumed to be negligible, and the effects of

deformation of the canopy is negligibly small. Thirdly, it was assumed that wind was uniform across the entire body of the parachute.

3.3 Parachute design

All tests were conducted using hemispherical parachute designs which were modelled using a CAD software, SOLIDWORKS. Physical prototypes were also designed using the following calculations which describe the dimensions for each gore of a 6 gore hemispherical parachute.

The reference area was determined using the standard formula for drag coefficient, $C_d = \frac{F_D}{0.5\rho v^2 s}$. The radius is thus calculated for the final diameter to be found. The entire height of the gore was split into 20 points as seen in fig 3.3a, with the width at each point found using the formula, $w = \frac{d\,\pi\,cos\,4.5n^\circ}{6}$, where d is the diameter and n is the point number. Vent ratio was varied, at 0%, 3%, 5%, and 7%. Fig 3.3b shows the dimensions of the final parachutes tested.

Fig 3.3c shows a scaled down prototype of the parachute canopy was made using paper to act as a proof of concept, verifying that the method above was effective in producing a hemispherical parachute.

The canopy of the actual parachute was made with a non-porous polyester fabric which was cut to scale for the gores of each canopy. The 6 gores were eventually sewn together to form the complete canopies. Symmetry was maintained as much as possible to minimise errors occurring from unaccounted movement in the parachute during flight. Fig 3.3d shows the final parachutes that were tested.

Fig 3.3e shows the 3D payload box made using PLA material and was used to store the components of the payload including the Arduino Nano 33 BLE board which acted as the motherboard and IMU, which were wired to a SD card module as seen in Fig 3.3f, as well as the batteries and battery holder which acted as the power source. Some bluetack was also added to the payload as additional mass such that the payload would have a more regular mass of 0.25 kg for simpler calculations.

3.4 CFD Simulations

Flow field of the surrounding fluid of the parachute during descent was numerically simulated. Fig 3.4 shows the mesh of the parachute and the control volume which was made at a ratio of 1:4 based on past works. The simulation platform was Ansys Student 2023R2. SST K OMEGA was chosen for turbulent modelling to replicate real-life conditions where there is a high probability of turbulence due to environmental factors such as the physical terrain or other man-made structures. The assumptions made in the simulation were that the parachute cannot deform, and no heat was exchanged with the surroundings, with the velocity of steady incoming air flow set as 5 ms^{-1}, with the density of air being 1.225 kg/m^3.

3.5 Experimental Drop-Test

Real-life drop tests were then conducted for each variation of the parachute from a height of 9.2m, travelling vertically downwards in a straight line.

3.6 Data collection

The Arduino Nano 33 BLE microcontroller was integrated into our experimental setup for an efficient and reliable collection of data, and was selected due to its Bluetooth Low Energy (BLE) capabilities for a seamless interface between its equipped sensors and external devices. The BLE capabilities were harnessed by defining a custom BLE service and characteristic tailored to our experimental needs, leveraging upon its accelerometer and gyroscope sensors (LSM6DS3) to facilitate data collection. Fig 3.6 displays the code used to programme the Arduino Nano 33 BLE board to collect data for the experiment, based on C/C^{++} language.

The Arduino Nano 33 BLE microcontroller which comes with the LSM9DS1 Inertial Measurement Unit (IMU) was placed in the payload of the parachute and used to generate acceleration and angular velocity data in the axes of the Arduino board. Data was stored in the form of CSV in a micro SD card through a SD module and transferred to a laptop using a SD card reader.

3.7 Data Processing

Collected data was then processed by creating a directional cosine matrix (DCM) based on defined Euler angles of the parachute's coordinate system to relate the coordinate system of the parachute in reference to the earth axis. The acceleration in the 3 axes of the Arduino board was then multiplied by the DCM. The data was then processed by python using a directional cosine $matrix$ (DCM) shown below to convert data to the earth axes. This allows the forces and moments to be in the correct directions and the data can be properly analysed.

$$\mathbf{A}_X = \begin{bmatrix} 1 & 0 & 0 \\ 0 & \cos\phi & -\sin\phi \\ 0 & \sin\phi & \cos\phi \end{bmatrix} \quad \mathbf{A}_Y = \begin{bmatrix} \cos\theta & 0 & \sin\theta \\ 0 & 1 & 0 \\ -\sin\theta & 0 & \cos\theta \end{bmatrix} \quad \mathbf{A}_Z = \begin{bmatrix} \cos\psi & -\sin\psi & 0 \\ \sin\psi & \cos\psi & 0 \\ 0 & 0 & 1 \end{bmatrix}$$

4. Results

4.1a Effect of vent ratio on drag

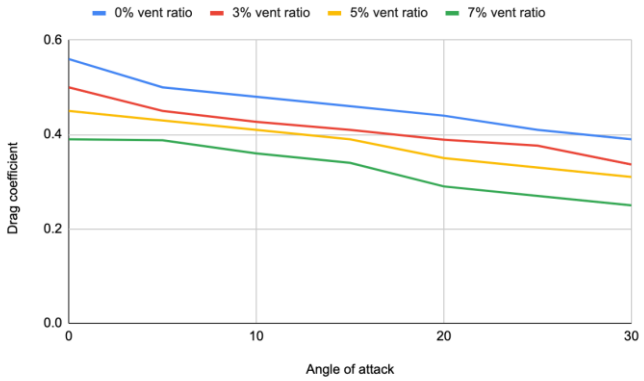

Fig 4.1.1 Graph of drag coefficient against vent ratio from CFD

Data generated suggest that an increase in the vent radius causes a decrease in overall drag coefficient. Increasing the vent ratio allows for the air trapped in the parachute to escape, resulting in a decrease in the pressure the parachute experiences. Therefore, a lower pressure results in a smaller drag overall. The drag coefficient at a 0% vent hole ratio was found to be 0.56. A further increase in the vent hole ratio to 5% causes a decrease in the drag coefficient, which was 0.45. The vent ratio further increased to 7% and experienced a drag coefficient of 0.39. Therefore, the drag must be considered when designing the vent ratio for the parachute. However, the effect of vent ratio on drag is not nearly as significant as its effects on the stability of the parachute.

4.1b Effect of vent ratio on stability

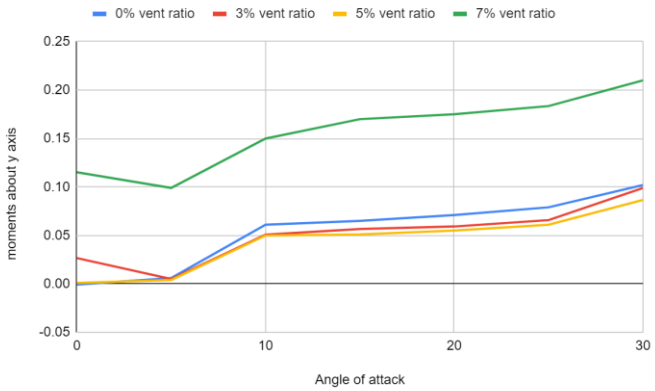

Fig 4.1.1 Graph of moments about y-axis against AOA at varying vent ratio from CFD

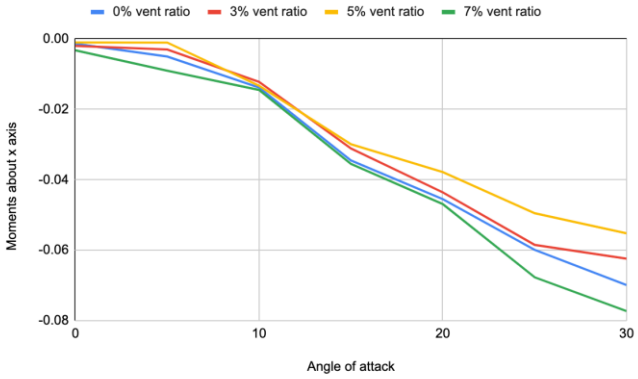

Fig 4.1.2 Graph of moments about x-axis against AOA at varying vent ratio from CFD

Moment graphs obtained from both experimental and numerical data highlight a correlating trend where an increase in vent ratio decreases moments of the parachute point where any further increase in the vent ratio increases moments of the parachute, introducing instability.

The vent ratio allows trapped turbulent air to escape through the parachute vent to increase stability, minimising the effects of turbulence and side forces on the parachute. By preventing excessive air pressure build-up, the risk of distortion of the parachute canopy can be effectively minimised. Experiments conducted show that the increased apex vent decreases the inflation of the canopy, preventing a shock load as the parachute opens that would cause shedding of

asymmetric wake vortices, causing the canopy to sway continuously. The results prove that vents play a crucial role in reducing oscillations and instabilities of the parachute during descent, as pressure is equalised on both sides of the parachute by allowing air to pass through the canopy, to minimise the risk of uneven inflation.

However, past an optimal vent ratio, it is shown that the parachute transitions into a phase of greater instability. This introduces greater risk of oscillations and irregularities in the parachute's flight path due to its increased susceptibility to wind, where the parachute experiences greater horizontal drift. Therefore, the vent ratio is important when designing a parachute to ensure stability

4.2a Effect of canopy size on drag

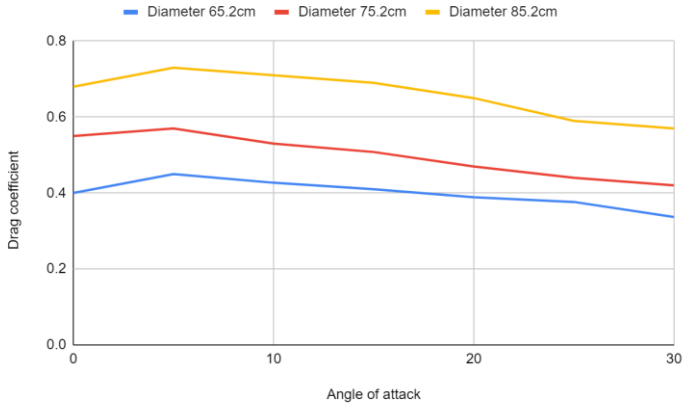

Fig 4.2.1 Graph of drag coefficient against canopy size from CFD

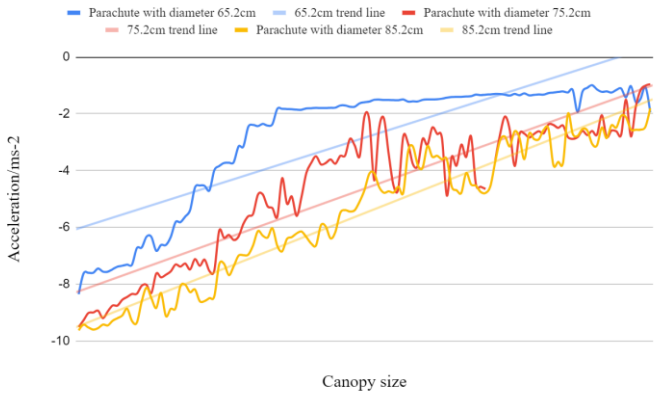

Fig 4.2.2 Graph of acceleration/ms^2 against time/s from experiments

The canopy size is directly proportional to the drag force experienced, $F_D = \frac{1}{2}\rho v^2 s$. Both numerical and experimental data show good agreement on this trend. This is expected as the effective area that the parachute is seeing is increased. This results in a larger area on which the

air resistance acts on, increasing the drag. Similarly, for angle of attack, when there is an increase in the angle of attack, the effective area is also reduced, resulting in a smaller drag.

Both numerical and experimental results show good agreement that the drag coefficient decreases at higher angles of attacks. At lower angles of attack, the parachute experiences more laminar flow. However, at higher angle of attacks, the adverse pressure gradients might lead to flow separation out of the parachute. Once separation occurs, it will lead to the formation of turbulent eddies and vortices. Shedding of such vortices in a periodic or quasi-periodic manner hence leads to vortex shedding, where under certain conditions, particularly in the context of bluff bodies with a large, non-streamlined shape such as in a parachute, can lead to a reduction of drag, further reducing drag at higher angle of attacks.

Greater deceleration suggests the parachute encounters greater drag, causing the downwards resultant force to decrease at a higher rate. The acceleration time graph shows the larger parachute with a larger magnitude of deceleration, thus encountering greater drag. The abrupt gradient of the deceleration profile of a larger parachute suggests the parachute experiences excessive turbulence, indicating inefficient drag production and greater drag.

4.2b Effect of canopy size on stability

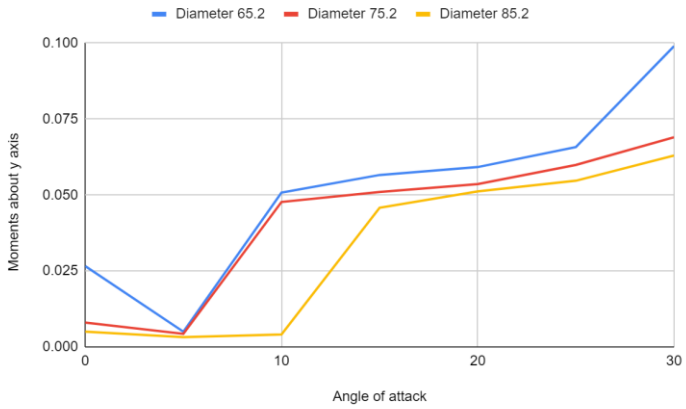

Fig 4.2.3. Moments about y-axis at varying canopy sizes from CFD

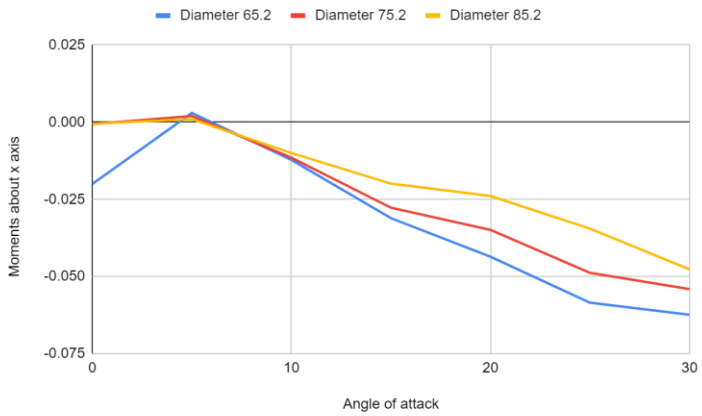

Fig 4.2.4. Moments about x-axis at varying canopy sizes from CFD

Experimental and numerical results in the moments graph in Fig 4.2.3 show good agreement in increased stability of the parachute at increased canopy sizes due to the increase in drag forces. Available literature shows that larger canopy sizes are characterised with enhanced pendulum stability, allowing a stable orientation, as increased drag forces dampen and provide a stabilising force to lateral disturbances, thus resisting horizontal motions in the parachute.

5. Discussion

5.1 Limitations

There were several key limitations which could have had detrimental effects on the experimental process. Unavoidable inconsistencies in the time intervals between data collection due to the processing speed and load shedding process of the Arduino which resulted in some time intervals varying by 1 or 12-13ms respectively at random points. Such inconsistencies may have affected the accuracy of data trends observed. The lack of a controlled environment meant that parachute movement could have been substantially influenced by wind patterns which could have resulted in some inaccurate findings. High sensitivity of the Arduino Nano 33 BLE sensor resulted in noisy data, which was minimised by repeating experiments. Real-life experiments also provided unavoidable factors such as the parachute not being fully rigid, and such deformations in the parachute could have affected the accuracy of data.

5.2 Error analysis

Numerically collected data from the CFD while ideal, models an unrealistic environment as it fails to accurately model real-world conditions such as wind patterns, leading to slight deviations in data collected, where drag coefficients were lower in CFD compared to experimentally collected data, as it fails to factor in effects such as turbulence from wind. However, error bars plotted against graphs of numerical and experimental data still show good correlation.

5.3 Further research

For the purpose of further or future research, it would be ideal for the test to be conducted using a more accurate and precise IMU in a controlled environment, using a fully rigid parachute to minimise any possible external factors which could affect the collected data.

6. Conclusion

Through a combination of numerical simulations and experimental tests, it was found that as vent ratio increases up to a certain point, parachute stability increased substantially while as canopy size increased, both drag coefficient and stability increased substantially. Meanwhile, as Angles of Attack increases, both drag coefficient and stability decreases substantially. The findings of this study strongly validate existing literature while also leaving room for further research in order to more precisely determine optimal parameters for parachutes of different applications as seen from the relationship between vent ratio and stability where there was a certain vent ratio beyond which stability began to decrease. It can be seen that there is an intricate balance that needs to be found between various parameters given that aerodynamic characteristics are complex and interrelated.

7. Bibliography

1. Ginn, J. M. (2014, December 2). Parachute dynamic stability and the effects of apparent inertia. https://www.ssdl.gatech.edu/sites/default/files/ssdl-files/papers/mastersProjects/GinnJ-8900.pdf
2. Halstrom, L. (2021, February). *Aerodynamic, moving-mesh modeling of parachute pendulum motion: Development and validation of a CFD methodology*. eScholarship, University of California. https://escholarship.org/uc/item/63q5t79v
3. Dobrokhodov, V. N., Yakimenko, O. A., & Junge, C. J. (2012, May 22). *Six-degree-of-freedom model of a controlled circular parachute*. Six-Degree-of-Freedom Model of a Controlled Circular Parachute. https://arc.aiaa.org/doi/10.2514/2.3143
4. Gunasinghe, S., Dilas, K. A., Sandaruwan, D., & Weerasinghe, M. (2017). A real-time 6DOF computational model to simulate RAM-air parachute dynamics. https://www.researchgate.net/publication/315151906_A_Real-Time_6DOF_Computational_Model_to_Simulate_Ram-Air_Parachute_Dynamics
5. Zhang, S., Sun, Z., & Yu, L. (2022, October 6). *Prediction and effect analysis for equilibrium profile of flexible ...* Prediction and effect analysis for equilibrium profile of flexible porous canopy fabric. https://journals.sagepub.com/doi/10.1177/15280837221109640?icid=int.sj-full-text.citing-articles.2
6. Ma1, A., Zhou2, S., Wu3, Q., & Zhu4, C. (2022, March). *IOPscience*. Journal of Physics: Conference Series. https://iopscience.iop.org/article/10.1088/1742-6596/2230/1/012017
7. Akash, H., Raj, S. A., Sathish, D., Kumar, A. A., & Balaji, H. (2021, May 3). *Design and computational analysis of Da Vinci Parachute Design in steady and unsteady flow with varying vent hole ratio*. International Journal of Research in Engineering, Science and Management. https://journal.ijresm.com/index.php/ijresm/article/view/689
8. Cao, Y., & Wei, N. (2020, August 25). *Flight trajectory simulation and aerodynamic parameter identification of large-scale parachute*. International Journal of Aerospace Engineering. https://www.hindawi.com/journals/ijae/2020/5603169/
9. Dawoodian, M., Dadvand, A., & Hassanzadeh, A. (2013, August 18). *A numerical and experimental study of the aerodynamics and stability of a horizontal parachute*. International Scholarly Research Notices. https://www.hindawi.com/journals/isrn/2013/320563/

8. Appendix

Fig 3.3a Gore

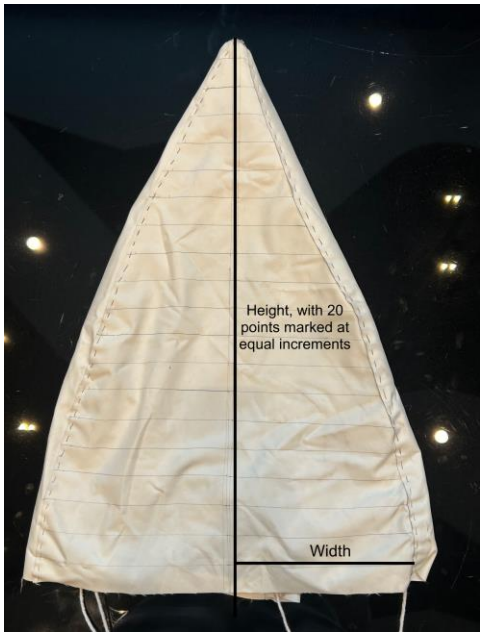

Fig 3.3b Dimensions of tested parachute

	Diameter/cm	**Suspension line/cm**	**Vent diameter/cm**
Parachute 1	65.2	74.98	11.3
Parachute 2	75.2	86.48	13.0
Parachute 3	85.2	97.98	14.8
Parachute 4	65.2	74.98	0
Parachute 5	65.2	74.98	14.6
Parachute 6	65.2	74.98	17.3

Fig 3.3c Paper prototype

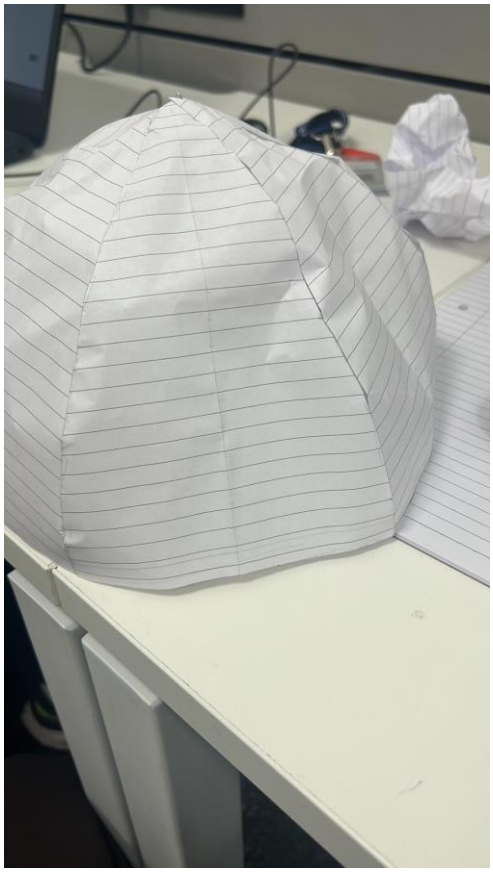

Fig 3.3d Final parachutes

P1	P2	P3
		

Fig 3.3e Payload Box

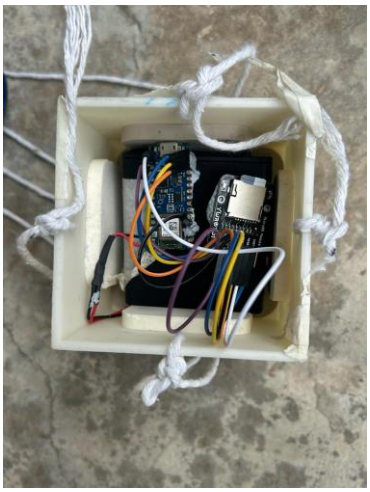

Fig 3.3f Wiring of Arduino with SD card module

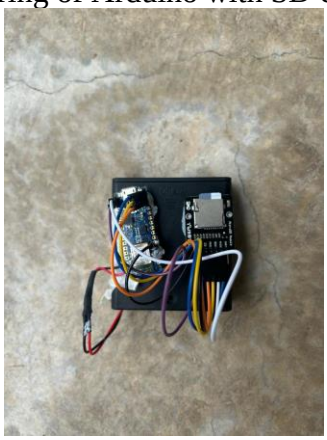

Fig 3.4a Mesh of Parachute

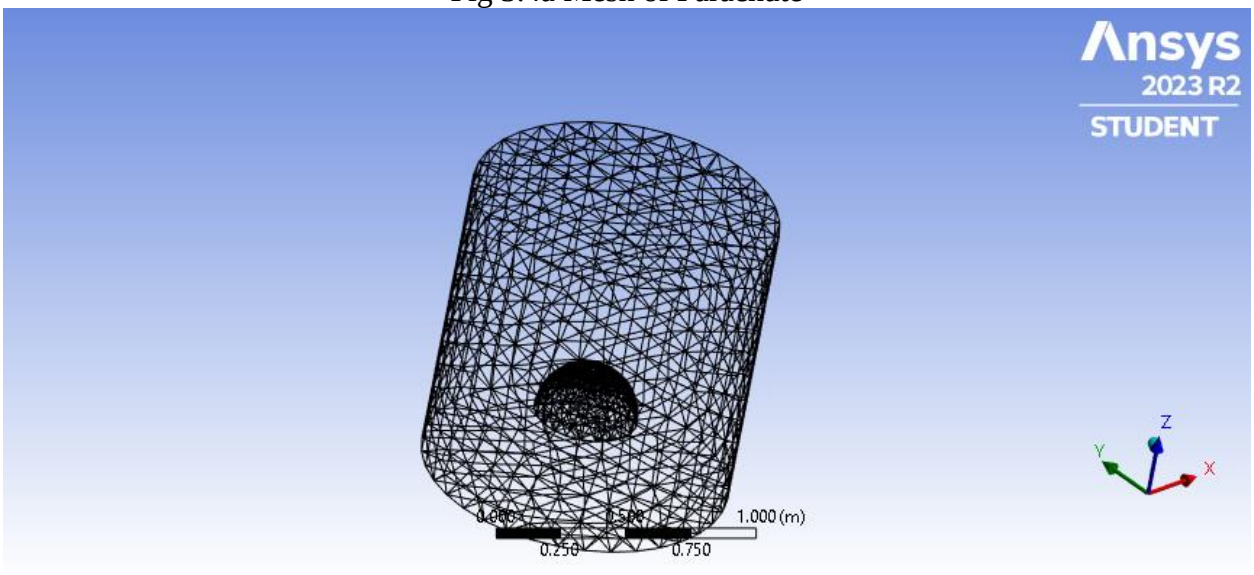

Fig 3.6 Arduino BLE 33 Code

```
#include <SPI.h>
#include <SD.h>
#include <Arduino_LSM9DS1.h>

const int chipSelect = 10;

float x, y, z;
int degreesX = 0;
int degreesY = 0;

float a, b, c;
int plusThreshold = 30, minusThreshold = -30;

void setup() {
  Serial.begin(2400);
  while (!Serial && millis() < 100);
    //Serial.println("Started");
    //Serial.print("Initializing SD card...");

  if (!SD.begin(chipSelect)) {
      //Serial.println("initialization failed. Things to check:");
      //Serial.println("1. is a card inserted?");
      //Serial.println("2. is your wiring correct?");
      //Serial.println("3. did you change the chipSelect pin to match your
shield or module?");
      //Serial.println("Note: press reset button on the board and reopen
this serial monitor after fixing your issue!");
      while (1);
    }
    //Serial.println("initialization done.");


  if (!IMU.begin()) {
    //Serial.println("Failed to initialize IMU!");
    while (1);
  }

  //Serial.print("Gyroscope sample rate = ");
  //Serial.print(IMU.gyroscopeSampleRate());
  //Serial.println(" Hz");
  //Serial.println();
  //Serial.println("Gyroscope in degrees/second");
  //Serial.println("A\tB\tC");

  //Serial.print("Accelerometer sample rate = ");
  //Serial.print(IMU.accelerationSampleRate());
  //Serial.println("Hz");

  File dataFile = SD.open("datalog.txt", FILE_WRITE);
  dataFile.println();
  dataFile.println("starting new test");
  dataFile.close();
```

```
  //Serial.println("moving to loop");

}

void loop() {

   delay(20);

  File dataFile = SD.open("datalog.txt", FILE_WRITE);
  // log milliseconds since starting
  uint32_t m = millis();

  //Serial.print(m);         // milliseconds since start
  //Serial.print(", ");
  int t = m;

  if (IMU.accelerationAvailable()) {
  IMU.readAcceleration(x, y, z);

  }
   if (IMU.gyroscopeAvailable()) {
    IMU.readGyroscope(a, b, c);


   // if the file is available, write to it:

}
  String dataString = String(t) + "," + String(x) + "," + String(y)+ "," +
String(z) + "," +String(a) + "," + String(b)+ "," + String(c);
   // File dataFile = SD.open("datalog.txt", FILE_WRITE);
   if (dataFile) {
    dataFile.println(dataString);
    dataFile.close();
    // print to the serial port too:
    //Serial.println(dataString);
  }else {
    //Serial.println("error opening datalog.txt");
  }
}
```

Fig 4.3a Pressure contour graphs at varying angle of attacks

AOA 5	AOA 10

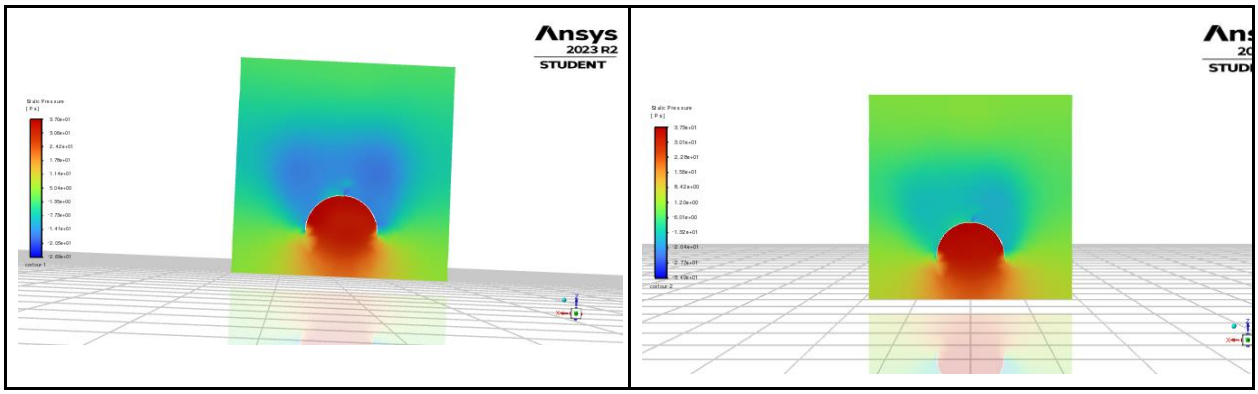

AOA 15	AOA 20

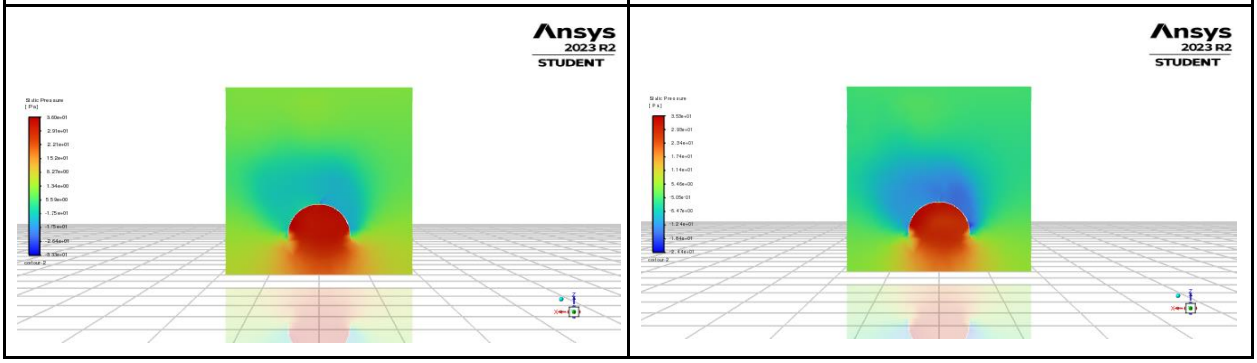

AOA 25	AOA 30

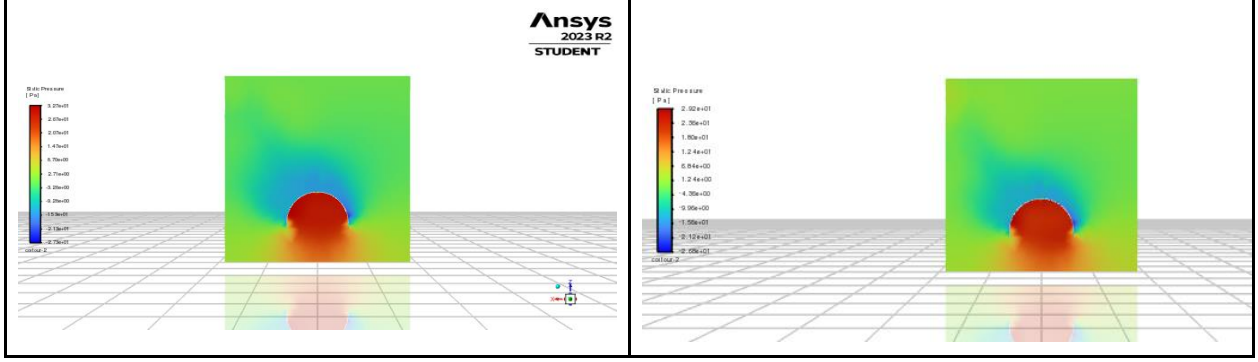

Fig 4.3b Velocity contour graphs at varying angle of attacks

AOA 5	AOA 10

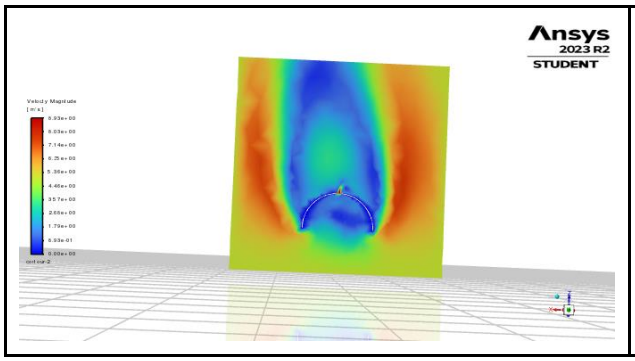

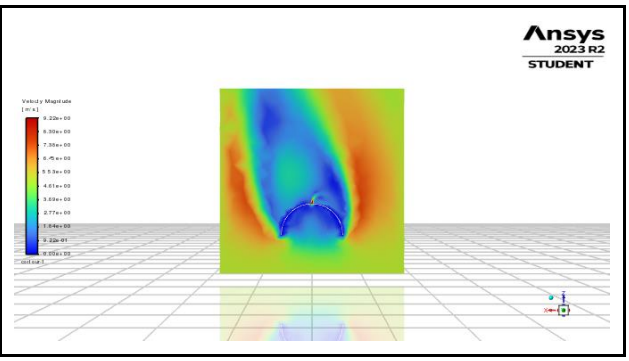

AOA 15	AOA 20
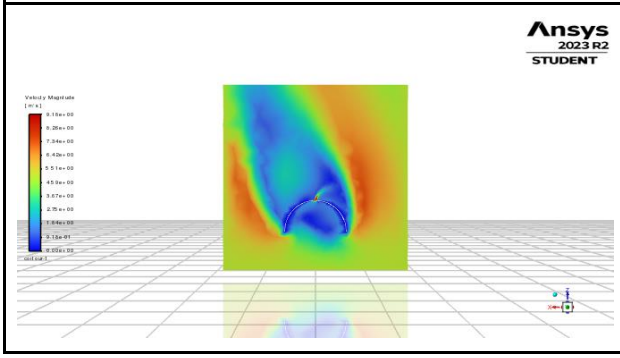	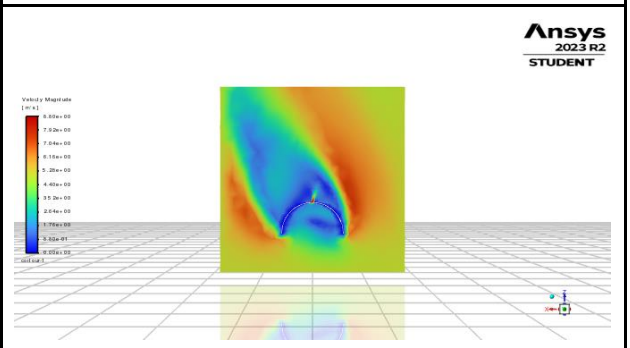

AOA 25	AOA 30